



Variations in initial $^{26}\text{Al}/^{27}\text{Al}$ ratios among fluffy Type A Ca–Al-rich inclusions from reduced CV chondrites

Noriyuki Kawasaki^{a,e,*}, Changkun Park^b, Naoya Sakamoto^c, Sun Young Park^b, Hyun Na Kim^d, Minami Kuroda^e, Hisayoshi Yurimoto^{e,c,a}

^a Institute of Space and Astronautical Science, Japan Aerospace Exploration Agency, Sagamihara 252-5210, Japan

^b Division of Earth-System Sciences, Korea Polar Research Institute, Incheon 21990, Republic of Korea

^c Isotope Imaging Laboratory, Creative Research Institution, Hokkaido University, Sapporo 001-0021, Japan

^d Department of Geoenvironmental Sciences, Kongju National University, Chungcheongnam-do 32588, Republic of Korea

^e Natural History Sciences, Hokkaido University, Sapporo 060-0810, Japan

ARTICLE INFO

Article history:

Received 29 October 2018

Received in revised form 11 January 2019

Accepted 14 January 2019

Available online 1 February 2019

Editor: F. Moynier

Keywords:

Ca–Al-rich inclusions

Al–Mg systematics

secondary ion mass spectrometry

early Solar System

ABSTRACT

Al–Mg mineral isochrons of three Ca–Al-rich inclusions (CAIs) that formed primarily by condensation, one fine-grained, spinel-rich inclusion and two fluffy Type A CAIs, from the reduced CV chondrites Efremovka and Vigarano were obtained by *in situ* Al–Mg isotope measurements using secondary ion mass spectrometry. The slope of the isochron obtained for the fine-grained, spinel-rich inclusion gives an initial $^{26}\text{Al}/^{27}\text{Al}$ value, $(^{26}\text{Al}/^{27}\text{Al})_0$, of $(5.19 \pm 0.17) \times 10^{-5}$. This is essentially identical to the Solar System initial $^{26}\text{Al}/^{27}\text{Al}$ determined by whole-rock Al–Mg isochron studies for CAIs in CV chondrites. In contrast, the isochron slopes for the two fluffy Type A CAIs from their Al–Mg mineral isochrons, $(4.703 \pm 0.082) \times 10^{-5}$ and $(4.393 \pm 0.084) \times 10^{-5}$, are significantly lower than the Solar System initial value. The range of $(^{26}\text{Al}/^{27}\text{Al})_0$ values of the three CAIs, from (5.19 ± 0.17) to $(4.393 \pm 0.084) \times 10^{-5}$, corresponds to a formation age spread of 0.17 ± 0.04 Myr. This formation age spread is similar to that of igneous CAIs from CV chondrites. The data suggest that condensation and melting of minerals occurred in the hot nebular gas contemporaneously for ~ 0.2 Myr at the very beginning of our Solar System, if ^{26}Al was distributed homogeneously in the CAI forming region. Alternatively, the observed variations in $(^{26}\text{Al}/^{27}\text{Al})_0$ among fluffy Type A CAIs would also raise a possibility of heterogeneous distributions of ^{26}Al in the forming region.

© 2019 Elsevier B.V. All rights reserved.

1. Introduction

Ca–Al-rich inclusions (CAIs) in chondrites are the oldest objects formed in our Solar System, as determined by U-corrected Pb–Pb absolute chronology (Connelly et al., 2012). CAIs are composed of minerals that predicted to be high-temperature equilibrium condensate minerals from the solar nebular gas (e.g., Grossman, 1972). Volatility-fractionated trace-element patterns (Boynton, 1975; Davis and Grossman, 1979) and complex multi-layered structures (Wark and Lovering, 1977) of fine-grained, spinel-rich inclusions (FGIs) in CV chondrites are indicative of condensates formed directly from the solar nebular gas. FGIs in the reduced CV chondrites, such as Efremovka and Leoville, preserve

the original mineral assemblages formed by condensation. These assemblages consist mainly of spinel, melilite, anorthite, and aluminous diopside, and more rarely perovskite and hibonite (Krot et al., 2004), however, in FGIs from oxidized CV chondrite such as Allende, original anorthite and melilite have been replaced by secondary minerals such as nepheline and sodalite (MacPherson, 2014). Coarse-grained CAIs in CV chondrites are petrographically sub-classified into Types A, B, and C (MacPherson, 2014 and references therein). Compact Type A, Type B, and Type C CAIs experienced melting and solidification and are thus igneous in origin (e.g., MacPherson and Grossman, 1981; Wark and Lovering, 1982; Wark, 1987; Yurimoto et al., 1998), but fluffy Type A CAIs (FTA CAIs) were never extensively melted (e.g., MacPherson and Grossman, 1984; Beckett and Stolper, 1994; Grossman et al., 2002; Kawasaki et al., 2017). FTA CAIs generally show irregular shapes with aggregate structures and are composed mainly of gehlenitic melilite (MacPherson and Grossman, 1984; Katayama et al., 2012; Kawasaki et al., 2012). The melilite crystals in FTA CAIs commonly

* Corresponding author. Present address: Natural History Sciences, Hokkaido University, Sapporo 060-0810, Japan.

E-mail address: kawasaki@ep.sci.hokudai.ac.jp (N. Kawasaki).

show reverse zoning, with åkermanite-rich cores and gehlenite-rich rims, which likely formed by gas–solid condensation, and do not display signatures of later extensive melting (MacPherson and Grossman, 1984; Katayama et al., 2012; Park et al., 2012; Kawasaki et al., 2017).

Lee et al. (1976) first showed that CAIs contained live ^{26}Al , a short-lived radionuclide with a half-life of 0.705 Myr (Norris et al., 1983), at the time of their formation. The source of ^{26}Al in the Solar System is still being debated (e.g., Krot et al., 2012 and references therein), but direct evidences or constraints deciphering it have not been obtained so far. It is suggested that ^{26}Al was homogeneously distributed throughout at least the region of the Solar System where “canonical” CAIs in CV chondrites formed (e.g., MacPherson et al., 1995; Jacobsen et al., 2008; Larsen et al., 2011). For this reason the initial abundance of ^{26}Al has been widely used to determine relative chronology of the early Solar System (e.g., Kita et al., 2013 and references therein). It should be noted that, however, the presence of ^{26}Al -poor refractory objects such as CAIs with Fractionation and Unidentified Nuclear isotopic effects (FUN CAIs) in CV chondrites (e.g., Wasserburg et al., 1977; Holst et al., 2013; Park et al., 2017 and references therein), corundum grains in carbonaceous and unequilibrated ordinary chondrites (Makide et al., 2011), grossite- and hibonite-rich CAIs in CH and CH/CB chondrites (e.g., Krot et al., 2008), and hibonite-rich CAIs in CM chondrites (e.g., Kööp et al., 2016 and references therein) implies heterogeneous distributions of ^{26}Al in the CAI-forming region at the very beginning of the Solar System evolution.

Recent high-precision Al–Mg mineral isochron studies using secondary ion mass spectrometry (SIMS) offer detailed distributions of initial $^{26}\text{Al}/^{27}\text{Al}$ values, $(^{26}\text{Al}/^{27}\text{Al})_0$, for individual CAIs in the CV chondrites (e.g., MacPherson et al., 2010, 2012, 2017; Kita et al., 2012; Kawasaki et al., 2015, 2017, 2018; Park et al., 2017). These data show that unmelted CAIs such as FGIs, FTA CAIs, and amoeboid olivine aggregates (AOAs), exhibit consistent $(^{26}\text{Al}/^{27}\text{Al})_0$ values of $\sim 5.2 \times 10^{-5}$, whereas igneous CAIs such as compact Type A and Type B CAIs exhibit a range of values from ~ 5.2 to $\sim 4.2 \times 10^{-5}$. This corresponds to a formation age spread of ~ 0.2 Myr. Reversely zoned melilite crystals in a FTA CAI V2-01 from the reduced CV chondrite Vigarano, however, yield mineral isochrons with $(^{26}\text{Al}/^{27}\text{Al})_0$ of $\sim 4.7 \times 10^{-5}$, corresponding to intermediate values among the values for igneous CAIs, even though they are unmelted crystals (Kawasaki et al., 2017). Few studies have obtained such high-precision Al–Mg mineral isochrons for the unmelted CAIs; only one FGI, two FTA CAIs, and one AOA have been examined (MacPherson et al., 2010, 2012; Kawasaki et al., 2017). In this study, we used high-precision SIMS to obtain Al–Mg mineral isochrons for two CAIs from the reduced CV chondrite Efremovka, a FTA CAI (named HKE01, Kawasaki et al., 2012) and a FGI (HKE02). The isochrons enable a more systematic comparison of $(^{26}\text{Al}/^{27}\text{Al})_0$ between CAIs formed by condensation and by melt crystallization than has previously been achieved. We also performed an Al–Mg isotope measurement of the åkermanite-rich core of a reversely zoned melilite crystal in FTA CAI V2-01 that has $(^{26}\text{Al}/^{27}\text{Al})_0$ of $\sim 4.7 \times 10^{-5}$ (Kawasaki et al., 2017) for a better estimation of its initial $^{26}\text{Mg}^*$ value, $(^{26}\text{Mg}^*)_0$. The precise estimation of $(^{26}\text{Mg}^*)_0$ helps to discuss whether the Al–Mg mineral isochron have evolved in single stage or not. The preliminary results of this work were reported by Kawasaki and Yurimoto (2017).

2. Experimental techniques

2.1. Sample preparation and elemental analysis

Both the FTA CAI HKE01 and the FGI HKE02 are found in a polished thin section of the reduced CV chondrite Efremovka

(Fig. 1). The FTA CAI V2-01 is included in a polished thin section of the reduced CV chondrite Vigarano (Katayama et al., 2012; Kawasaki et al., 2017). The polished thin sections were coated with a carbon thin film (~ 10 – 20 nm) for backscattered electron (BSE) imaging, elemental analyses using an energy dispersive X-ray spectrometer (EDS), electron backscatter diffraction (EBSD) mapping, and *in situ* Al–Mg isotope measurement in peak-jumping mode using SIMS. The carbon coated sections were overlaid with a gold thin film (~ 70 nm) for *in situ* Al–Mg isotope measurement in multicollection mode using SIMS. The gold film is effective for charge compensation in the multicollection mode to minimize instrumental mass fractionations.

BSE imaging, quantitative elemental analysis, and X-ray elemental mapping were conducted for the three CAIs in this study using field emission type scanning electron microscopes with energy dispersive X-ray spectrometers (FE-SEM-EDS; JEOL JSM-7000F with Oxford X-Max 150 at Hokkaido University and Hitachi SU6600 with Oxford X-Max 20 at Japan Aerospace Exploration Agency). A 15 keV electron beam probe with currents of 0.3 nA (for quantitative analysis) and 5–13 nA (for mapping) was employed for JSM-7000F + X-Max 150 and a 15 keV electron beam probe with currents of 0.9 nA (for quantitative analysis) and 30 nA (for mapping) was employed for SU6600 + X-Max 20 in this study. Bulk Al/Mg chemical compositions of FTA CAIs were estimated as an average of multiple measurements covering the entire CAIs using a rastered electron beam. Crystal orientation mapping of the CAI minerals was performed using an EBSD system (AZtec HKL) equipped with the FE-SEM (JEOL JSM-7000F) at Hokkaido University, with a 20 keV electron beam probe and a current of 4 nA, to determine grain boundaries of each crystalline mineral. Qualitative X-ray elemental mapping was performed simultaneously with the EBSD crystal orientation mapping.

2.2. Al–Mg isotope measurements

Mg-isotopes and $^{27}\text{Al}/^{24}\text{Mg}$ ratios of the CAI minerals in this study were measured using a Cameca ims-1280HR SIMS at Hokkaido University. An $^{16}\text{O}^-$ primary beam accelerated to 23 keV was employed in the experiment. We used both the peak-jumping mode and the multicollection mode, depending on the secondary ion intensities of Mg-isotopes from the minerals.

2.2.1. Multicollection mode for low Al/Mg minerals

For analysis of Al-poor melilite ($^{27}\text{Al}/^{24}\text{Mg} < \sim 16$), diopside, and spinel, the Mg-isotopes ($^{24}\text{Mg}^+$, $^{25}\text{Mg}^+$, and $^{26}\text{Mg}^+$) and $^{27}\text{Al}^+$ were measured simultaneously in multicollection mode with four Faraday cups (FCs): $^{24}\text{Mg}^+$ for L2* (10^{11} Ω), $^{25}\text{Mg}^+$ for L1 (10^{11} Ω), $^{26}\text{Mg}^+$ for H1 (10^{11} Ω), and $^{27}\text{Al}^+$ for H2* (10^{10} Ω). The primary beam current was set to 21–40 nA with an elliptical shape of 20 – 25×25 – 30 μm for measurements of Al-poor melilite to ensure similar secondary Mg ion intensities from regions with different chemical compositions. A 3.8–7.4 nA beam with an elliptical shape of 6 – 11×8 – 17 μm was used for the diopside and spinel measurements. The mass resolution ($M/\Delta M$) was set to ~ 2000 , which is sufficient to prevent the contribution of ion interferences (e.g., $^{48}\text{Ca}^{2+}$, $^{24}\text{MgH}^+$, $^{25}\text{MgH}^+$, and $^{52}\text{Cr}^{2+}$) on Mg-isotopes. The secondary ion intensities of $^{24}\text{Mg}^+$ were 0.4 – 1.0×10^8 , 1.0 – 1.3×10^8 and 1.4 – 1.8×10^8 cps for Al-poor melilite, diopside, and spinel, respectively. Each measurement consisted of 20 cycles of counting the secondary ions for 10 s. Obtained count rates were corrected for the FC background and the relative yield of each detector. The relative sensitivity factors (RSFs) for Al/Mg were determined through measurements of a synthetic melilite glass, Takashima augite, and Russian spinel for Al-rich melilite, diopside, and spinel, respectively. The $\delta^{25}\text{Mg}$ values of the CAI minerals were calculated

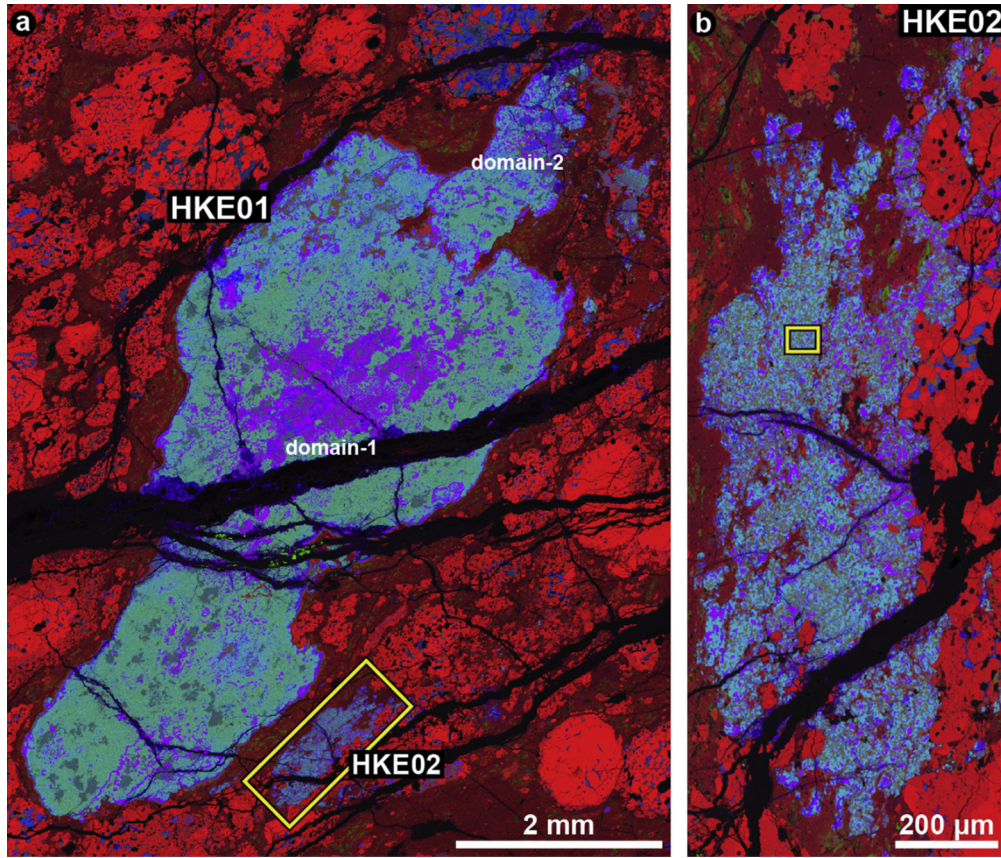


Fig. 1. Combined X-ray elemental map of (a) fluffy Type A CAI HKE01 and (b) fine-grained CAI HKE02 from Efremovka. Mg is shown in red, Ca is shown in green, and Al is shown in blue. The yellow box in (a) indicates the area shown in (b). The yellow box in (b) indicates the area shown in Fig. 2. (For interpretation of the colors in the figure(s), the reader is referred to the web version of this article.)

assuming that the $\delta^{25}\text{Mg}$ of those synthetic and natural standards is zero.

2.2.2. Peak-jumping mode for Al-rich melilites

For Al-rich melilite ($^{27}\text{Al}/^{24}\text{Mg} > \sim 16$), Mg-isotopes ($^{24}\text{Mg}^+$, $^{25}\text{Mg}^+$, and $^{26}\text{Mg}^+$) were measured using an axial electron multiplier, while $^{27}\text{Al}^+$ was measured using an axial Faraday cup or using a multicollector Faraday cup ($10^{11} \Omega$, designed for H2^*) simultaneously with $^{25}\text{Mg}^+$, with the peak-jumping mode of a sector magnet. An $^{16}\text{O}^-$ primary beam accelerated to 23 keV was adjusted to 0.2–0.8 nA for each spot, according to variations in chemical composition, to obtain sufficient secondary Mg ion intensities, resulting in an elliptical beam shape measuring $\sim 5 \times 7 \mu\text{m}$. The secondary ion intensities of $^{24}\text{Mg}^+$ were $1.2\text{--}3.1 \times 10^5$ cps. $M/\Delta M$ was set at ~ 4000 , which is sufficient to resolve ion interferences (e.g., $^{48}\text{Ca}^{2+}$, $^{24}\text{MgH}^+$, $^{25}\text{MgH}^+$, and $^{52}\text{Cr}^{2+}$) from $^{24}\text{Mg}^+$, $^{25}\text{Mg}^+$, and $^{26}\text{Mg}^+$. Each measurement was conducted for 50 cycles of a counting sequence with $^{24}\text{Mg}^+$ for 3 s, $^{25}\text{Mg}^+$ for 10 s, $^{26}\text{Mg}^+$ for 10 s, and $^{27}\text{Al}^+$ for 1 s when $^{27}\text{Al}^+$ was measured using the axial Faraday cup and for 100 cycles of a counting sequence with $^{24}\text{Mg}^+$ for 2 s, $^{25}\text{Mg}^+$ for 2 s, $^{25}\text{Mg}^+$ and $^{27}\text{Al}^+$ for 4 s, and $^{26}\text{Mg}^+$ for 6 s when $^{27}\text{Al}^+$ was measured using the multicollector FC H2^* . Obtained count rates were corrected for the FC background, the EM deadtime, and the relative yield of each detector.

2.2.3. Radiogenic excess ^{26}Mg

The radiogenic excess ^{26}Mg , $\delta^{26}\text{Mg}^*$, was calculated using an exponential fractionation law with the exponent $\alpha_{\text{natural}} = 0.5128$, because natural fractionation for Mg-isotopes is considered to be controlled by evaporation processes (Davis et al., 2015). We deter-

mined the instrumental mass fractionation, α_{SIMS} , for the calculation of excess radiogenic ^{26}Mg through measurements of terrestrial standards, a synthetic melilite glass, a synthetic fassaite glass, Takashima augite, and Russian spinel. In this study, seven measurements were made of α_{SIMS} for melilite (0.499 ± 0.004 (2σ), 0.464 ± 0.004 , 0.540 ± 0.004 , 0.515 ± 0.003 , 0.523 ± 0.003 , 0.524 ± 0.003 , and 0.532 ± 0.003), four measurements were made for diopside (0.501 ± 0.009 , 0.512 ± 0.004 , 0.514 ± 0.004 , and 0.520 ± 0.005), and three measurements were made for spinel (0.516 ± 0.005 , 0.512 ± 0.004 , and 0.511 ± 0.003). The instrumental offset, β , ranged from -0.55 to -0.31 with 2σ errors of $0.01\text{--}0.03$, depending on the minerals and the analytical sessions. The fractionation-corrected $\delta^{26}\text{Mg}^*$ values for CAI minerals were determined by the following equation

$$\begin{aligned} \delta^{26}\text{Mg}^* &= \delta^{26}\text{Mg}_{\text{sample}} - \left[\left(1 + \frac{\delta^{25}\text{Mg}_{\text{sample}}}{1000} \right)^{\frac{1}{\alpha_{\text{natural}}}} - 1 \right] \times 1000 \\ &\quad - \beta + \left[\left(1 + \frac{\delta^{25}\text{Mg}_{\text{std}}}{1000} \right)^{\frac{1}{\alpha_{\text{natural}}}} - 1 \right] \times 1000 \\ &\quad - \left[\left(1 + \frac{\delta^{25}\text{Mg}_{\text{std}}}{1000} \right)^{\frac{1}{\alpha_{\text{SIMS}}}} - 1 \right] \times 1000, \end{aligned}$$

where $\delta^{25,26}\text{Mg}_{\text{sample}} = [({}^{25,26}\text{Mg}/{}^{24}\text{Mg})_{\text{sample}} / ({}^{25,26}\text{Mg}/{}^{24}\text{Mg})_{\text{ref.}} - 1] \times 1000$ and $\delta^{25}\text{Mg}_{\text{std}} = [({}^{25}\text{Mg}/{}^{24}\text{Mg})_{\text{std}} / ({}^{25}\text{Mg}/{}^{24}\text{Mg})_{\text{ref.}} - 1] \times 1000$. Details of the correction procedures and the error estimations are described elsewhere (Kawasaki et al., 2017). The analyt-

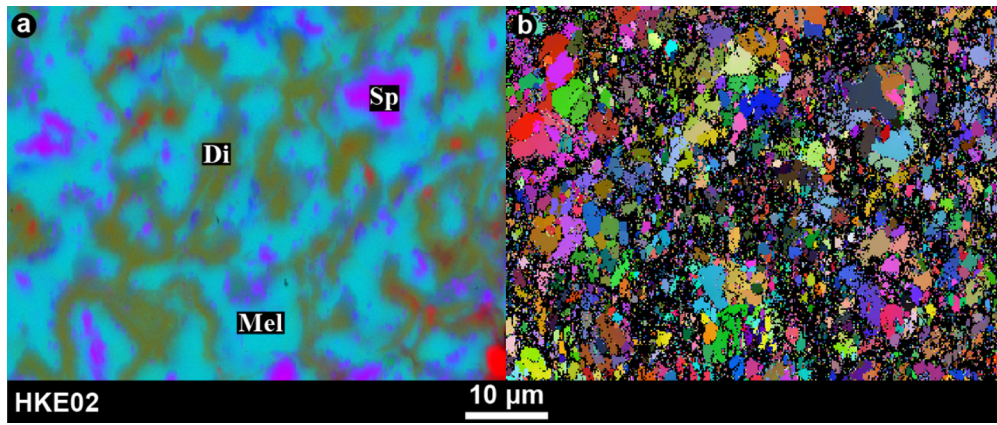


Fig. 2. Representative textures of HKE02. (a) Combined X-ray elemental map in the area indicated by the yellow box in Fig. 1b, showing Mg (red), Ca (green), and Al (blue). (b) Electron backscatter diffraction (EBSD) Euler map of the same area displayed in (a). Di, diopside; Mel, melilite; Sp, spinel.

ical errors (2σ) for $\delta^{26}\text{Mg}^*$ were 0.11–0.28‰ for Al-poor melilite, 0.11–0.14‰ for diopside, and 0.11–0.15‰ for spinel, respectively.

The calculation methods for $\delta^{26}\text{Mg}^*$ and $\delta^{25}\text{Mg}$ were essentially the same in both analytical modes, although α_{SIMS} and β were not determined in the peak-jumping mode because the instrumental mass fractionation and the natural mass fractionation were indistinguishable from each other under the measurement conditions used here. The analytical errors for $\delta^{26}\text{Mg}^*$ for Al-rich melilite were assigned as internal errors (2SE) and were 0.9–1.9‰.

3. Results

3.1. Petrography

HKE02 is a fine-grained, spinel-rich inclusion in the polished section of Efremovka with a greatest dimension of ~ 1.7 mm (Fig. 1b), located near the FTA CAI HKE01 (Fig. 1a). HKE02 has an irregular shape and complex multi-layered textures composed mainly of spinel, melilite, and diopside (Figs. 1b and 2), consistent with textures of previously reported fine-grained, spinel-rich inclusions from the reduced CV chondrites (Krot et al., 2004). Anorthite and perovskite are observed as accessory minerals. The crystal sizes of spinel, diopside, and melilite are mainly a few micrometers across and generally less than $10\ \mu\text{m}$ across (Fig. 2b). Melilite has narrow variations in chemical composition ranging from $\sim \text{Åk}4$ to $\sim \text{Åk}10$, where $\text{Åk}\# = \text{Mg} \times 100 / (\text{Mg} + \text{Al}/2)$. Relatively large spinel grains ($\sim 10\ \mu\text{m}$) have FeO contents of less than 1.0 wt% and $\text{Fe}/(\text{Mg} + \text{Fe})$ ratios of ~ 0.01 , while the edges of the spinel grains and the smaller spinel grains show higher contents of FeO up to ~ 20 wt% due to secondary processes on the parent body. In this study, Al–Mg isotopic compositions were only measured for the spinels with low FeO. Representative mineral chemical compositions are shown in Table S1.

The FTA CAI HKE01 has a greatest dimension of ~ 10 mm and an irregular shape (Fig. 1a). A detailed petrographic description of HKE01 and chemical and O-isotopic distributions of melilite crystals are presented in Kawasaki et al. (2012). HKE01 is composed of two domains divided by Wark–Lovering (W–L) rims (Wark and Lovering, 1977), which grew in nebular reservoirs with distinct O-isotopic compositions, temperatures and/or pressures (Kawasaki et al., 2012). Each domain has a core–mantle structure. At one of the two domains (termed “domain-2” by Kawasaki et al., 2012), the mantle consists mainly of numerous reversely zoned melilite crystals that are likely nebular condensates, similar to the general petrography of FTA CAIs (MacPherson and Grossman, 1984). The crystal sizes of the reversely zoned melilite crystals mainly fall within a range from several micrometers to a few tens of micrometers (Kawasaki et al., 2012). Since this study focuses on $(^{26}\text{Al}/^{27}\text{Al})_0$

at condensation, we only present the Al–Mg isotopic compositions of reversely zoned melilite crystals and W–L rim minerals in domain-2 of HKE01. Spinel in the W–L rim typically have low FeO contents (less than 1.0 wt%) and $\text{Fe}/(\text{Mg} + \text{Fe})$ ratios (~ 0.01). In this study, we only measured the Al–Mg isotopic composition of spinels with these low FeO contents because a small amount of spinel has higher contents of FeO up to ~ 15 wt% due to secondary processes on the parent body. Representative chemical compositions of minerals in the W–L rim and spinel in the CAI interior are shown in Table S2. The bulk $^{27}\text{Al}/^{24}\text{Mg}$ ratio of domain-2 of HKE01 is estimated to be 4.6.

The FTA CAI V2-01 has a greatest dimension of ~ 7 mm and is irregularly shaped. A detailed petrographic description of V2-01 and the chemical, O- and Al–Mg isotopic compositions of minerals are presented in Katayama et al. (2012) and Kawasaki et al. (2017). The CAI is mainly composed of reversely zoned melilite crystals and a W–L rim surrounds the entire CAI. The bulk $^{27}\text{Al}/^{24}\text{Mg}$ ratio of V2-01 is estimated to be 5.9.

3.2. Al–Mg isotopic compositions

The Mg-isotopic data and measured $^{27}\text{Al}/^{24}\text{Mg}$ ratios for the minerals in the FGI and the two FTA CAIs are given in Table 1 and plotted on Al–Mg isochron diagrams in Figs. 3–5; also shown are the Al–Mg isotope data of melilite in V2-01 from Kawasaki et al. (2017). The data for all three inclusions yield very well-correlated isochrons. The slope of the regression line for HKE02 (Fig. 3) gives $(^{26}\text{Al}/^{27}\text{Al})_0 = (5.19 \pm 0.17) \times 10^{-5}$ and $(\delta^{26}\text{Mg}^*)_0 = 0.022 \pm 0.087\%$ (2σ uncertainties). The regression line for reversely zoned melilite crystals in HKE01 gives $(^{26}\text{Al}/^{27}\text{Al})_0 = (4.37 \pm 0.13) \times 10^{-5}$ and $(\delta^{26}\text{Mg}^*)_0 = 0.029 \pm 0.084\%$, and that for V2-01 gives $(^{26}\text{Al}/^{27}\text{Al})_0 = (4.64 \pm 0.12) \times 10^{-5}$ and $(\delta^{26}\text{Mg}^*)_0 = 0.10 \pm 0.19\%$ (Fig. 4). Including the data for minerals from the W–L rim in HKE01 gives $(^{26}\text{Al}/^{27}\text{Al})_0 = (4.393 \pm 0.084) \times 10^{-5}$ and $(\delta^{26}\text{Mg}^*)_0 = 0.022 \pm 0.042\%$, and for V2-01 gives $(^{26}\text{Al}/^{27}\text{Al})_0 = (4.703 \pm 0.082) \times 10^{-5}$ and $(\delta^{26}\text{Mg}^*)_0 = -0.060 \pm 0.032\%$ (Fig. 5).

4. Discussion

4.1. Mass fractionation correction

An exponential fractionation law with the exponent $\alpha_{\text{natural}} = 0.5128$, determined by vacuum evaporation experiments of CAI-like liquids (Davis et al., 2015), was used for calculations of $\delta^{26}\text{Mg}^*$ in this study and in Kawasaki et al. (2017). If instead of 0.5128 we use the exponent 0.511 in the kinetic exponential fractionation law (e.g., Jacobsen et al., 2008; Larsen et al., 2011;

Table 1
Magnesium-isotopic compositions (‰) and $^{27}\text{Al}/^{24}\text{Mg}$ ratios of minerals in HKE02, HKE01, and V2-01.

Minerals	$^{27}\text{Al}/^{24}\text{Mg}$	2σ	$\delta^{26}\text{Mg}^*$	2σ	$\delta^{25}\text{Mg}$	2σ	Minerals	$^{27}\text{Al}/^{24}\text{Mg}$	2σ	$\delta^{26}\text{Mg}^*$	2σ	$\delta^{25}\text{Mg}$	2σ
<i>HKE02</i>							Mel	29.1	1.1	9.4	1.9	3.9	1.3
Mel	46.8	1.0	16.5	1.9	2.0	1.6	Mel	26.0	1.0	8.2	1.9	4.3	1.3
Mel	49.7	0.8	18.4	1.3	1.6	1.6	Mel	25.4	1.1	7.4	1.1	1.6	1.0
Mel	45.9	1.7	17.1	1.9	-0.2	1.7	Mel	18.7	0.8	6.1	1.0	1.0	1.0
Mel	40.1	0.9	15.6	0.9	-0.3	1.1	Mel	28.7	1.3	8.3	1.8	8.2	1.5
Mel	38.5	0.3	14.0	1.4	1.5	1.3	Mel	29.6	0.2	9.2	1.4	4.4	0.8
Mel	37.5	1.1	13.7	1.4	-0.6	1.4	Mel	28.2	0.4	8.6	1.7	4.2	1.5
Mel	39.9	0.6	14.8	1.3	-1.4	1.3	Mel	27.2	0.3	7.5	1.6	6.6	1.4
Mel	29.3	0.5	10.9	1.7	0.6	1.2	Mel	32.2	0.2	10.3	1.2	5.6	1.1
Mel	28.4	0.2	10.6	1.1	-0.1	0.8	Mel	24.6	0.1	7.5	1.3	5.7	1.1
Mel	34.9	0.2	13.1	1.2	1.2	0.9	Mel	32.7	0.4	10.0	1.3	6.1	1.5
Sp	2.59	0.00	1.03	0.13	2.01	0.11	Mel	21.1	0.2	6.9	1.6	0.5	1.5
Sp	2.61	0.01	0.97	0.16	2.31	0.04	Mel	27.8	0.2	9.8	1.3	2.5	1.1
Sp	2.60	0.01	0.97	0.12	2.31	0.13	Mel	6.99	0.01	2.35	0.20	7.66	0.09
<i>HKE01, domain-2</i>							Mel	6.69	0.01	2.09	0.20	7.54	0.08
Mel	7.20	0.02	2.17	0.15	7.95	0.07	Mel	5.78	0.02	1.89	0.13	6.47	0.05
Mel	8.47	0.06	2.62	0.13	8.19	0.07	Mel	6.70	0.01	2.14	0.13	7.02	0.07
Mel	7.59	0.03	2.41	0.14	6.85	0.07	Mel	6.42	0.02	1.93	0.15	7.27	0.07
Mel	11.55	0.10	3.82	0.28	2.04	0.14	Mel	8.67	0.05	2.82	0.14	8.34	0.11
Mel	12.49	0.03	3.94	0.26	7.34	0.12	Mel	6.11	0.03	1.96	0.11	7.36	0.09
Mel	19.84	0.07	6.45	0.19	2.02	0.10	Mel	7.20	0.04	2.29	0.12	7.09	0.10
Mel	25.5	0.7	7.2	1.7	3.4	1.6	Di	0.14	0.00	-0.01	0.13	-0.85	0.07
Mel	28.1	0.4	7.7	1.6	4.7	1.4	Di	0.37	0.02	0.14	0.14	-1.19	0.06
Mel	44.6	0.4	14.4	1.5	8.1	1.3	Di	0.44	0.01	0.12	0.13	-1.07	0.07
Mel	16.7	0.4	5.6	1.7	5.6	1.5	Di	0.47	0.00	0.11	0.11	-1.17	0.05
Mel	26.3	0.4	7.8	1.4	5.5	1.3	Di	0.85	0.02	0.18	0.13	-0.97	0.06
Mel	43.5	0.4	13.1	1.1	7.3	1.3	Sp	2.52	0.00	0.87	0.15	1.93	0.05
Mel	43.6	0.5	13.6	1.3	3.2	1.0	Sp	2.53	0.00	0.93	0.11	0.74	0.05
Mel	41.2	0.4	12.1	1.3	3.4	1.3	Sp	2.50	0.00	0.90	0.11	1.82	0.08
Mel	27.7	0.2	8.3	1.5	4.4	1.1	<i>V2-01, grain 1</i>						
Mel	33.3	0.5	10.3	1.3	8.2	0.9	Mel	7.40	0.01	2.57	0.20	7.61	0.09
Mel	40.9	1.7	12.1	1.9	3.3	1.3							

Di: diopside, Mel: melilite, Sp: spinel.

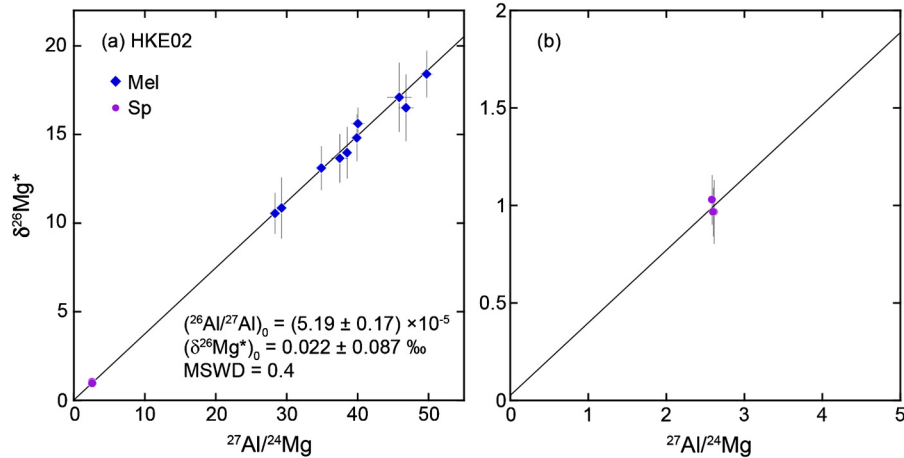


Fig. 3. Al-Mg mineral isochron for HKE02. (b) exhibits spinel data in (a). Here and in Figs. 4 and 5, Isoplot Model 1 (Ludwig, 2003) was used to fit isochrons. Errors are 2σ . Symbols without error bars have errors smaller than their symbol sizes. Mel, melilite; Sp, spinel.

Wasserburg et al., 2012), the initial values inferred from the slopes of the regression lines become $(^{26}\text{Al}/^{27}\text{Al})_0 = (5.20 \pm 0.17) \times 10^{-5}$ and $(\delta^{26}\text{Mg}^*)_0 = 0.004 \pm 0.087\text{‰}$ for HKE02, $(^{26}\text{Al}/^{27}\text{Al})_0 = (4.39 \pm 0.13) \times 10^{-5}$ and $(\delta^{26}\text{Mg}^*)_0 = -0.012 \pm 0.084\text{‰}$ for melilite in HKE01, $(^{26}\text{Al}/^{27}\text{Al})_0 = (4.66 \pm 0.12) \times 10^{-5}$ and $(\delta^{26}\text{Mg}^*)_0 = 0.06 \pm 0.19\text{‰}$ for melilite in V2-01, $(^{26}\text{Al}/^{27}\text{Al})_0 = (4.366 \pm 0.084) \times 10^{-5}$ and $(\delta^{26}\text{Mg}^*)_0 = 0.015 \pm 0.042\text{‰}$ for both melilite and W-L rim minerals in HKE01, and $(^{26}\text{Al}/^{27}\text{Al})_0 = (4.690 \pm 0.082) \times 10^{-5}$ and $(\delta^{26}\text{Mg}^*)_0 = -0.055 \pm 0.032\text{‰}$ for both melilite and W-L rim minerals in V2-01 (Tables S3 and S4; Figs. S1–S3). The changes in the initial values of each regression line by this change in exponents fall within the analytical errors, respectively, although the values of $(\delta^{26}\text{Mg}^*)_0$ calculated using the exponent of 0.511 appear to be systematically lower than those calculated

using the exponent of 0.5128, due to heavy mass-dependent Mg-isotopic fractionations (Table 1; Kawasaki et al., 2017). The choice of exponents is insignificant for the discussion in this paper.

4.2. Al-Mg isotopic systematics

4.2.1. Spinel-rich FGI HKE02

The inferred initial values of $(^{26}\text{Al}/^{27}\text{Al})_0 = (5.19 \pm 0.17) \times 10^{-5}$ and $(\delta^{26}\text{Mg}^*)_0 = 0.022 \pm 0.087\text{‰}$ for the FGI HKE02 by the Al-Mg mineral isochron (Fig. 3) are indistinguishable from the whole-rock CAI values of $(^{26}\text{Al}/^{27}\text{Al})_0 = (5.23 \pm 0.13) \times 10^{-5}$ and $(\delta^{26}\text{Mg}^*)_0 = -0.040 \pm 0.029\text{‰}$ (Jacobsen et al., 2008) and $(^{26}\text{Al}/^{27}\text{Al})_0 = (5.252 \pm 0.019) \times 10^{-5}$ and $(\delta^{26}\text{Mg}^*)_0 = -0.0159 \pm 0.0014\text{‰}$ (Larsen et al., 2011). The initial values determined

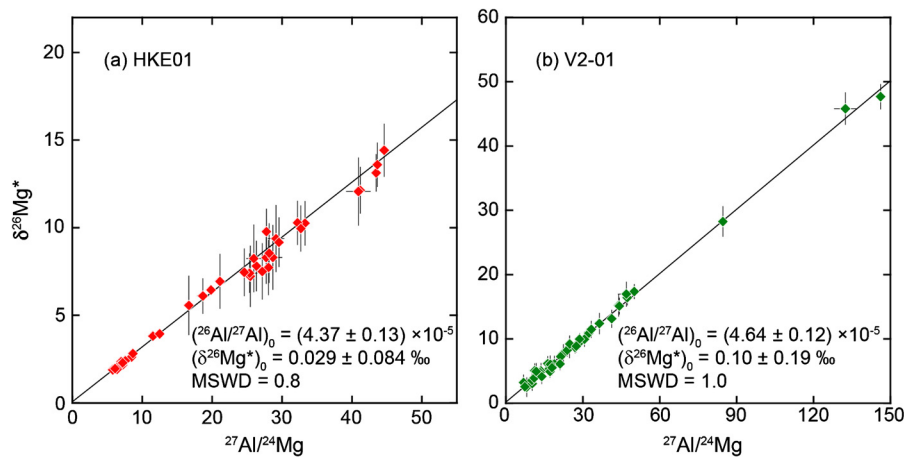


Fig. 4. Al–Mg mineral isochrons for reversely zoned melilite crystals in (a) HKE01 and (b) V2-01. Al–Mg isotope data for V2-01 minerals, except for one datum listed in Table 1, are from Kawasaki et al. (2017). Errors are 2σ . Symbols without error bars have errors smaller than their symbol sizes.

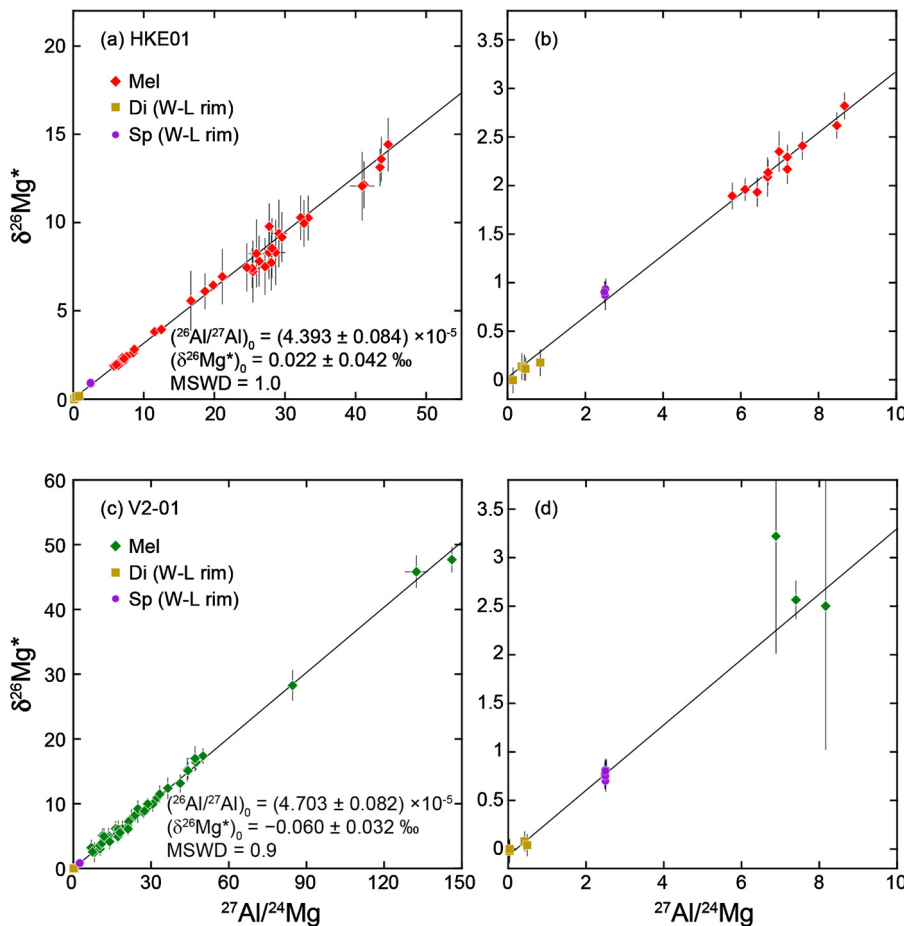


Fig. 5. Al–Mg mineral isochrons for reversely zoned melilite crystals and Wark–Lovering rim minerals in (a, b) HKE01 and in (c, d) V2-01. (b) and (d) show data with low Al/Mg ratio in (a) and (c), respectively. Al–Mg isotope data for V2-01 minerals, except for one datum listed in Table 1, are from Kawasaki et al. (2017). Errors are 2σ . Symbols without error bars have errors smaller than their symbol sizes. Di, diopside; Mel, melilite; Sp, spinel; W–L rim, Wark–Lovering rim.

here are also identical to the values determined for unmelted CAIs by *in situ* Al–Mg mineral isochron studies: $(^{26}\text{Al}/^{27}\text{Al})_0 = (5.27 \pm 0.17) \times 10^{-5}$ and $(\delta^{26}\text{Mg}^*)_0 = 0.02 \pm 0.06\text{‰}$ for a FGI from the reduced CV chondrite Leoville (MacPherson et al., 2010), $(^{26}\text{Al}/^{27}\text{Al})_0 = (5.29 \pm 0.28) \times 10^{-5}$ and $(\delta^{26}\text{Mg}^*)_0 = -0.07 \pm 0.11\text{‰}$ for a FTA CAI from Vigarano (MacPherson et al., 2012), and $(^{26}\text{Al}/^{27}\text{Al})_0 = (5.13 \pm 0.11) \times 10^{-5}$ and $(\delta^{26}\text{Mg}^*)_0 = -0.020 \pm 0.015\text{‰}$ for an AOA from Vigarano (MacPherson et al., 2012).

4.2.2. FTA CAI HKE01

Reversely zoned melilite crystals in domain-2 of HKE01 are likely to have primarily formed individually by condensation from the nebular gas and then aggregated to form the CAI (Kawasaki et al., 2012). The condensation origin of reversely zoned melilite crystals in Type A CAIs are supported by an abrupt change of O-isotopic compositions at crystal boundary of melilite in an Al-lende compact Type A CAI ON01 (Park et al., 2012) and Mg-isotope distributions in melilite crystals in V2-01 (Kawasaki et al., 2017;

details are in Section 4.2.3), because these O- and Mg-isotopic signatures are very unlikely to be explained by melt crystallization processes.

If the growth of individual crystals was slow enough, the gehlenitic, high $^{27}\text{Al}/^{24}\text{Mg}$ -side of the melilite data would show a depleted $^{26}\text{Mg}^*$ composition relative to the linear isochronous correlation between $^{27}\text{Al}/^{24}\text{Mg}$ and $\delta^{26}\text{Mg}^*$ on the Al–Mg isochron diagram, owing to the decay of ^{26}Al in the nebular gas from which they condensed. However, there are no systematic depletions of $\delta^{26}\text{Mg}^*$ in the HKE01 melilite data (Fig. 4a). The mineral isochron of the reversely zoned melilite crystals can be defined to have initial values of $(^{26}\text{Al}/^{27}\text{Al})_0 = (4.37 \pm 0.13) \times 10^{-5}$ and $(\delta^{26}\text{Mg}^*)_0 = 0.029 \pm 0.084\%$.

The inferred $(^{26}\text{Al}/^{27}\text{Al})_0$ for HKE01 melilite, $(4.37 \pm 0.13) \times 10^{-5}$, is significantly lower than the best estimate for Solar System initial $^{26}\text{Al}/^{27}\text{Al}$ (Jacobsen et al., 2008; Larsen et al., 2011), and lower also than $(^{26}\text{Al}/^{27}\text{Al})_0$ in other primitive unmelted CAIs (MacPherson et al., 2010, 2012) and FGI HKE02 (this work). The difference in $(^{26}\text{Al}/^{27}\text{Al})_0$ between the FTA CAI HKE01 and the FGI HKE02 is analytically robust since they are mounted in the same thin section of Efremovka (Fig. 1a) and some of the measurements of the melilite crystals in both the CAIs were conducted during the same sessions. Thus, it is highly implausible that analytical artifacts could have produced the difference in $(^{26}\text{Al}/^{27}\text{Al})_0$ between them (e.g., due to incorrect RSFs for Al/Mg).

An alternative explanation for the discrepancy might be late disturbances of the ^{26}Al – ^{26}Mg system of HKE01 melilite after their condensation and aggregation to form HKE01. These late disturbances might be caused by (1) re-heating processes below solidus temperatures in the solar nebula, (2) partial melting in the solar nebula, and (3) thermal metamorphism in the asteroidal parent body of the Efremovka meteorite. Especially by (1) and (2), the ^{26}Al – ^{26}Mg system could have reset in a closed system to record $(^{26}\text{Al}/^{27}\text{Al})_0$ at the timing of these processes, if the complete resetting of the ^{26}Al – ^{26}Mg system occurred.

Melilite crystals in HKE01 exhibit significant variations of mass-dependent Mg-isotopic fractionations, ranging from $\sim -1\%$ to $\sim 8\%$ in $\delta^{25}\text{Mg}$ (Table 1; Fig. S4). If the ^{26}Al – ^{26}Mg system of HKE01 melilite once had completely reset, yielding a well-defined isochron (Fig. 4a), $\delta^{25}\text{Mg}$ values of the melilite have been homogenized (i.e. the HKE01 melilite should show constant $\delta^{25}\text{Mg}$ values, in contrast to the observations). This suggests that there are no significant disturbances of ^{26}Al – ^{26}Mg system of the HKE01 melilite by (1) re-heating processes below solidus temperatures and (2) partial melting in the solar nebula. These heating processes might have partially disturbed the ^{26}Al – ^{26}Mg system, however, we could say that such disturbances were involved in the uncertainties of our data even if they occurred.

On the other hand, (3) thermal metamorphism in the asteroidal parent body might cause Mg-isotope exchange between melilite crystals and adjacent minerals and/or matrix minerals, after the decay of significant amounts of ^{26}Al . However, the Mg-isotope exchange rate depends on grain size (e.g., Kawasaki et al., 2015 and references therein). Thus, we conclude that such late disturbances are unlikely, because the grain sizes of melilite crystals in domain-2 of HKE01 (mainly ranging from several micrometers to a few tens of micrometers; Kawasaki et al., 2012) are larger than those of melilite crystals in HKE02 (mainly ranging between a few micrometers and less than 10 μm ; Fig. 2b). The well-correlated isochronous relationship spanning wide variations in $^{27}\text{Al}/^{24}\text{Mg}$ ratio for the melilite data (Fig. 4a) also suggests that the late disturbances are implausible.

Our Al–Mg data infer that the ^{26}Al – ^{26}Mg system of HKE01 melilite preserve $(^{26}\text{Al}/^{27}\text{Al})_0$ at the timing of its condensation from the solar nebular gas despite of insignificant (negligible) disturbances of the ^{26}Al – ^{26}Mg system by reheating processes in the

solar nebula and/or in the asteroidal parent body. The Al–Mg mineral isochron of HKE01 melilite suggest a short time formation for the melilite crystals from the nebular gaseous reservoir with a homogeneous distribution of the initial abundance of ^{26}Al , within a time duration corresponding to the error of $(^{26}\text{Al}/^{27}\text{Al})_0$. The melilite crystals would have formed within 0.06 Myr.

Investigations of W–L rim minerals are useful to get more precise estimations of initial values of Al–Mg isotope systematics for the FTA CAI HKE01, by compiling W–L rim data with those in Fig. 4a discussed above. Although minerals in the W–L rims are proposed to have formed in multiple stages (e.g., Wark and Lovering, 1977; Krot et al., 2017 and references therein), the formation processes of the W–L rims can essentially be divided into two classes: the rims are either a product of condensation from the nebular gas (e.g., Simon et al., 2005; Bolser et al., 2016) or are inheritances from host CAIs that were involved in processes such as gas–solid reactions, evaporation and melting (e.g., MacPherson et al., 1981; Wark and Boynton, 2001; Wark, 2005).

In the case of a nebular gas origin for the W–L rim of HKE01, since the W–L rim should have formed later than the interior melilite crystals, the Al–Mg isotope data plots of the W–L rim minerals would deviate downward from the linear isochronous correlation displayed in Fig. 4a. The Al–Mg isotope data, however, show no significant deviations from an Al–Mg isochron regression line (Figs. 5a and 5b). Therefore, we recalculate initial values for HKE01 to be $(^{26}\text{Al}/^{27}\text{Al})_0 = (4.393 \pm 0.084) \times 10^{-5}$ and $(\delta^{26}\text{Mg}^*)_0 = 0.022 \pm 0.042\%$. These initial values are identical, within the analytical error, to those for the mineral isochron of the reversely zoned melilite crystals (Fig. 4a). Consequently, the CAI interior and W–L rim must have formed sequentially within a short period of time.

In the case of a reprocessed origin for the W–L rim of HKE01 as an inheritance from a host CAI, a resetting of the ^{26}Al – ^{26}Mg system should have occurred when the W–L rim formed. Therefore, the Al–Mg isotope data for the W–L rim minerals would deviate upward from the linear isochronous correlation displayed in Fig. 4a, because the resetting of the ^{26}Al – ^{26}Mg system would elevate their $\delta^{26}\text{Mg}^*$ values. However, as discussed above, all the Al–Mg isotope data plot on the isochron (Figs. 5a and 5b). Therefore, we recommend $(^{26}\text{Al}/^{27}\text{Al})_0 = (4.393 \pm 0.084) \times 10^{-5}$ and $(\delta^{26}\text{Mg}^*)_0 = 0.022 \pm 0.042\%$ as the best estimates of initial values for HKE01 at condensation. The difference in $(^{26}\text{Al}/^{27}\text{Al})_0$ between the FTA CAI HKE01 and the FGI HKE02 corresponds to a relative age difference of 0.17 ± 0.04 Myr.

4.2.3. FTA CAI V2-01

Kawasaki et al. (2017) examined the Al–Mg isotopic compositions of six reversely zoned melilite crystals in FTA CAI V2-01. They found three patterns of mass-dependent Mg-isotopic fractionations within the melilite crystals along directions of crystal growth; the $\delta^{25}\text{Mg}$ values of two crystals tended to decrease along directions of crystal growth, the $\delta^{25}\text{Mg}$ values of two crystals tended to increase, and two crystals had constant $\delta^{25}\text{Mg}$ values. The decreasing $\delta^{25}\text{Mg}$ values along directions of crystal growth shown by two of the crystals are inconsistent with a formation model for reversely zoned melilite crystals involving crystallization from incomplete melts with melt evaporation (Grossman et al., 2002), and are thus strong supporting evidence for the condensation origin of them (Kawasaki et al., 2017). In contrast, the increasing $\delta^{25}\text{Mg}$ values along directions of crystal growth in two of the crystals can be explained by both the model of crystallization from incomplete melts with melt evaporation and the model of condensation from the nebular gas (Kawasaki et al., 2017). In this study, we excluded the two crystals with increasing $\delta^{25}\text{Mg}$ values during crystal growth for ^{26}Al – ^{26}Mg

systematics because of the focus of study on $(^{26}\text{Al}/^{27}\text{Al})_0$ at condensation.

The individual Al–Mg mineral isochrons of the four reversely zoned melilite crystals, which are concluded to be of condensation origin, have identical $(^{26}\text{Al}/^{27}\text{Al})_0$ and $(\delta^{26}\text{Mg}^*)_0$ to each other within analytical error (Kawasaki et al., 2017). The Al–Mg isotope data of the four crystals (Kawasaki et al., 2017) and the newly obtained data for the Åk-rich core of one of the melilite crystals (Table 1) plot on a single straight line on the Al–Mg isochron diagram (Fig. 4b), whose slope corresponds to $(^{26}\text{Al}/^{27}\text{Al})_0 = (4.64 \pm 0.12) \times 10^{-5}$ and $(\delta^{26}\text{Mg}^*)_0 = 0.10 \pm 0.19\%$. As with the discussion in Section 4.2.2, the variations of mass-dependent Mg-isotope fractionations in the V2-01 melilite, ranging from $\sim 0\%$ to $\sim 9\%$ (Kawasaki et al., 2017), infer that the ^{26}Al – ^{26}Mg system of V2-01 melilite preserve $(^{26}\text{Al}/^{27}\text{Al})_0$ at the timing of its condensation from the solar nebular gas, without significant late disturbances of the ^{26}Al – ^{26}Mg system by any reheating processes.

An isochron regression line using the Al–Mg isotope data of both the melilite crystals and the W–L rim minerals in V2-01 gives initial values of $(^{26}\text{Al}/^{27}\text{Al})_0 = (4.703 \pm 0.082) \times 10^{-5}$ and $(\delta^{26}\text{Mg}^*)_0 = -0.060 \pm 0.032\%$ (Figs. 5c and 5d). All the data presented in Figs. 5c and 5d plot on the isochron and the inferred initial values are identical, within the analytical error, to those for the melilite isochron (Fig. 4b). The discussion in Section 4.2.2 applies equally well here; thus, we recommend $(^{26}\text{Al}/^{27}\text{Al})_0 = (4.703 \pm 0.082) \times 10^{-5}$ and $(\delta^{26}\text{Mg}^*)_0 = -0.060 \pm 0.032\%$ as the best estimates of initial values for V2-01 at condensation. The inferred $(^{26}\text{Al}/^{27}\text{Al})_0$ for V2-01 is also significantly lower than the $(^{26}\text{Al}/^{27}\text{Al})_0$ value of $\sim 5.2 \times 10^{-5}$. The difference in $(^{26}\text{Al}/^{27}\text{Al})_0$ between the FTA V2-01 and the FGI HKE02 corresponds to a relative age difference of 0.10 ± 0.04 Myr.

4.3. Variations in $(^{26}\text{Al}/^{27}\text{Al})_0$ among CAIs: contemporaneous occurrence of CAI condensation and CAI melting or heterogeneous distributions of ^{26}Al

Due to the decay of ^{26}Al to radiogenic ^{26}Mg , $^{26}\text{Mg}/^{24}\text{Mg}$ isotope ratios of minerals and bulk rocks evolve with time corresponding to their $^{26}\text{Al}/^{24}\text{Mg}$ ratios (i.e., $^{26}\text{Al}/^{27}\text{Al}$ and $^{27}\text{Al}/^{24}\text{Mg}$ ratios). High-precision Al–Mg mineral isochron data enable us to estimate, for each CAI, the timing of the last significant bulk Al/Mg chemical fractionation event caused by condensation and evaporation processes (MacPherson et al., 2012) and the model formation age (Kawasaki et al., 2015), if the CAI ^{26}Al – ^{26}Mg systems evolved in a closed system. The Mg-isotope evolution was primarily applied to the ^{26}Al – ^{26}Mg system of chondrules (Villeneuve et al., 2009).

The $(^{26}\text{Al}/^{27}\text{Al})_0$ and $(\delta^{26}\text{Mg}^*)_0$ for HKE02, HKE01, and V2-01 obtained by mineral isochrons are plotted on a diagram showing Mg-isotope evolution curves (Fig. 6). Since the validity of the Solar System initial $\delta^{26}\text{Mg}^*$ remains controversial (e.g., Kita et al., 2013), we plotted both the whole-rock CAI values determined by Jacobsen et al. (2008) and the values determined by Larsen et al. (2011). We discuss the Mg-isotope evolution of CAIs based on the values by Jacobsen et al. (2008) here, because the values reported by Jacobsen et al. (2008) entirely cover those of Larsen et al. (2011) due to the larger analytical errors.

The $(^{26}\text{Al}/^{27}\text{Al})_0$ and $(\delta^{26}\text{Mg}^*)_0$ for HKE02 are identical to the whole-rock CAI initial values within the analytical errors (Fig. 6), indicating that it formed from a gaseous reservoir whose Al–Mg isotopic composition was identical to that of the reservoir in which the CAIs used for whole-rock isochrons formed (Jacobsen et al., 2008; Larsen et al., 2011).

The $(^{26}\text{Al}/^{27}\text{Al})_0$ of $(4.393 \pm 0.084) \times 10^{-5}$ for HKE01 and the $(^{26}\text{Al}/^{27}\text{Al})_0$ of $(4.703 \pm 0.082) \times 10^{-5}$ for V2-01 are clearly lower than the whole-rock CAI $(^{26}\text{Al}/^{27}\text{Al})_0$. If we assume that the bulk Al/Mg chemical fractionation for HKE01 occurred at time “zero”

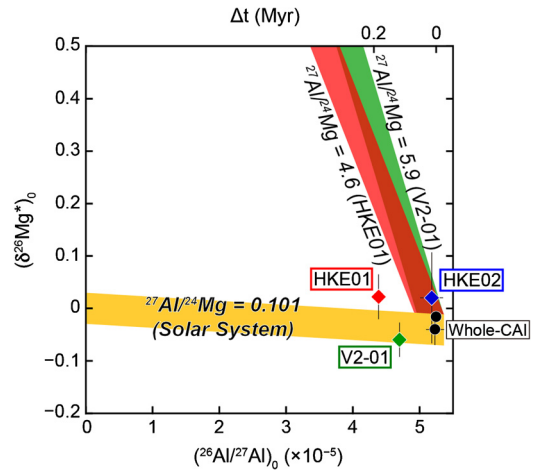


Fig. 6. Mg-isotope evolution of CAIs. Mg-isotope evolution curves from time “zero” (when $^{26}\text{Al}/^{27}\text{Al} = (5.23 \pm 0.13) \times 10^{-5}$) for HKE01 ($^{27}\text{Al}/^{24}\text{Mg} = 4.6$, red-colored area), V2-01 ($^{27}\text{Al}/^{24}\text{Mg} = 5.9$, green-colored area), and a solar-composition gas ($^{27}\text{Al}/^{24}\text{Mg} = 0.101$, yellow-colored area) are shown. If Al/Mg chemical fractionations for the CAIs occurred at time “zero”, Mg-isotopic compositions of the CAIs would have evolved with the bulk $^{27}\text{Al}/^{24}\text{Mg}$ ratios and thus would plot within the red-colored (HKE01) and green-colored (V2-01) areas. If instead CAIs condensed from the solar-composition gas, the Mg-isotopic compositions of CAIs would plot within the yellow-colored area. Whole-rock CAI values are from Jacobsen et al. (2008) and Larsen et al. (2011). The $^{27}\text{Al}/^{24}\text{Mg}$ ratio of the Solar System is taken from Lodders (2003). Errors are 2σ .

(when $^{26}\text{Al}/^{27}\text{Al} = (5.23 \pm 0.13) \times 10^{-5}$), the bulk Mg-isotopic composition of HKE01 would have evolved according to its own bulk $^{27}\text{Al}/^{24}\text{Mg}$ of 4.6 (Fig. 6). In that case, the $(\delta^{26}\text{Mg}^*)_0$ would be $0.23 \pm 0.06\%$ at the age corresponding to $^{26}\text{Al}/^{27}\text{Al} = (4.393 \pm 0.084) \times 10^{-5}$. The required $(\delta^{26}\text{Mg}^*)_0$ of $0.23 \pm 0.06\%$ deviates from the measured $(\delta^{26}\text{Mg}^*)_0$ of $0.022 \pm 0.042\%$ for HKE01. Similarly, the $(\delta^{26}\text{Mg}^*)_0$ of V2-01 would be $0.18 \pm 0.07\%$ at $^{26}\text{Al}/^{27}\text{Al} = (4.703 \pm 0.082) \times 10^{-5}$, which also deviates from the measured $(\delta^{26}\text{Mg}^*)_0$ of $-0.060 \pm 0.032\%$. However, the relationships between $(^{26}\text{Al}/^{27}\text{Al})_0$ and $(\delta^{26}\text{Mg}^*)_0$ for HKE01 and V2-01 are consistent with the Mg-isotope evolution curve of solar-composition gas (Fig. 6), suggesting these CAIs formed in an evolved nebula with solar-composition passed 0.1–0.2 Myr after the formation of HKE02.

Alternatively, if these CAIs formed contemporaneously with HKE02, distributions of ^{26}Al were heterogeneous in the forming region of FTA CAIs corresponding to a range over, at least, $4.4 \times 10^{-5} < (^{26}\text{Al}/^{27}\text{Al})_0 < 5.2 \times 10^{-5}$. The heterogeneous distributions of ^{26}Al in the CAI-forming region have been inferred from the presence of ^{26}Al -poor refractory objects, FUN CAIs in CV chondrites (e.g., Wasserburg et al., 1977; Holst et al., 2013; Park et al., 2017 and references therein), corundum grains in carbonaceous and unequilibrated ordinary chondrites (Makide et al., 2011), grossite- and hibonite-rich CAIs in CH and CH/CB chondrites (e.g., Krot et al., 2008), and hibonite-rich CAIs with large nucleosynthetic anomalies in ^{50}Ti and ^{48}Ca in CM chondrites (e.g., Kööp et al., 2016 and references therein). In addition, Al–Mg isotopic compositions of the bulk chondrites (Larsen et al., 2011) and U-corrected Pb–Pb age distributions for chondrules in carbonaceous and unequilibrated ordinary chondrites (Bollard et al., 2017) imply variable ^{26}Al abundances among inner solar protoplanetary disk solids. Among the ^{26}Al -poor refractory objects, $(\delta^{26}\text{Mg}^*)_0$ values have been well-determined only for the FUN CAIs, which exhibit large positive and negative anomalies of $(\delta^{26}\text{Mg}^*)_0$ (Park et al., 2017). Such large anomalies of $(\delta^{26}\text{Mg}^*)_0$ were not observed for HKE01 and V2-01 (Fig. 5). The variations in $(^{26}\text{Al}/^{27}\text{Al})_0$ among the FTA CAIs raise a possibility of heterogeneous distributions of ^{26}Al

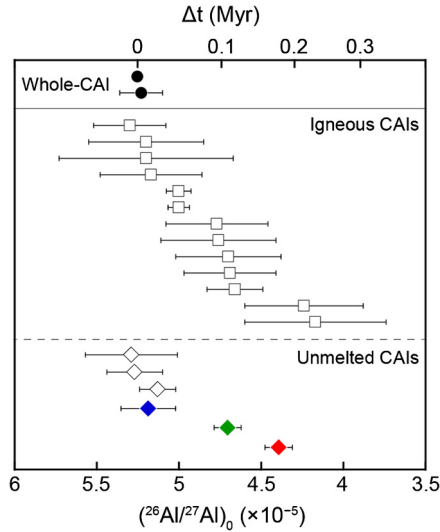


Fig. 7. Variations in initial $^{26}\text{Al}/^{27}\text{Al}$ values for igneous CAIs and for unmelted CAIs determined by high-precision mineral isochron studies. Initial $^{26}\text{Al}/^{27}\text{Al}$ values for igneous CAIs from the literature are shown for E60, E64, SJ101, F9, TS34, L3535, F4, V3137, 4N, TS35, F1, F6, and ALVIN, corresponding to the open squares from top to bottom (Kita et al., 2012; MacPherson et al., 2012; Kawasaki et al., 2018). Initial $^{26}\text{Al}/^{27}\text{Al}$ values for unmelted CAIs from the literature (open diamonds) are shown for F8, L3536, and F5 (MacPherson et al., 2010, 2012) and those from this study (colored diamonds) are shown for HKE02 (blue), V2-01 (green), and HKE01 (red). Whole-rock CAI initial $^{26}\text{Al}/^{27}\text{Al}$ values (black circles) are from Jacobsen et al. (2008) and Larsen et al. (2011). Errors are 2σ .

in the forming region of FTA CAIs, although we cannot fully conclude it from the present data set.

On the other hand, if these CAIs formed in a reservoir with different $(\delta^{26}\text{Mg}^*)_0$ from the Solar System initial value, precursors of HKE01 and V2-01 with non-solar $(\delta^{26}\text{Mg}^*)_0$ formed at time “zero” could have evolved to have the measured $(\delta^{26}\text{Mg}^*)_0$ by later resetting of their ^{26}Al – ^{26}Mg systems, although late disturbances of the ^{26}Al – ^{26}Mg systems for HKE01 and V2-01 melilites after condensation are suggested to be implausible from discussion in Sections 4.2.2 and 4.2.3. In that case, the reservoirs for these CAI precursors with non-solar $(\delta^{26}\text{Mg}^*)_0$ should have had $(\delta^{26}\text{Mg}^*)_0 = -0.25 \pm 0.07\%$ for HKE01 and $(\delta^{26}\text{Mg}^*)_0 = -0.28 \pm 0.07\%$ for V2-01. Such large negative non-solar $(\delta^{26}\text{Mg}^*)_0$ have been recognized only for FUN CAIs (Park et al., 2017 and references therein). The CAIs V2-01 and HKE01, however, do not show FUN CAI-like mass-dependent fractionations for O-isotope (Kawasaki et al., 2012, 2017; Katayama et al., 2012) and Mg-isotope (Kawasaki et al., 2017; Table 1; Fig. S4).

The $(^{26}\text{Al}/^{27}\text{Al})_0$ values for the three CAIs determined in this study range from (5.19 ± 0.17) to $(4.393 \pm 0.084) \times 10^{-5}$, which corresponds to a formation age spread of 0.17 ± 0.04 Myr. This formation age spread and the Mg-isotope evolutions for them infer that they formed from a nebular gaseous reservoir with solar-composition during the first ~ 0.2 Myr period of the earliest Solar System (Fig. 7). The variation range in $(^{26}\text{Al}/^{27}\text{Al})_0$ is consistent with that for the igneous CAIs (MacPherson et al., 2012, 2017; Kita et al., 2012; Kawasaki et al., 2018). These results suggest that condensation and melting of CAI minerals contemporaneously occurred in the early solar nebula during ~ 0.2 Myr, if ^{26}Al was homogeneously distributed in the forming region of these CAIs.

5. Conclusions

Newly obtained high-precision Al–Mg mineral isochrons of the fine-grained, spinel-rich inclusion HKE02 and the fluffy Type A CAIs HKE01 and V2-01 in the reduced CV chondrites revealed significant variations in $(^{26}\text{Al}/^{27}\text{Al})_0$ among the three CAIs. The in-

ferred $(^{26}\text{Al}/^{27}\text{Al})_0$ and $(\delta^{26}\text{Mg}^*)_0$ imply that their Mg-isotope systems evolved in a solar-composition nebular gas with $^{27}\text{Al}/^{24}\text{Mg} = 0.101$, from which they condensed, consistent with their condensation origin from the nebular gas. The inferred variation range in $(^{26}\text{Al}/^{27}\text{Al})_0$, from (5.19 ± 0.17) to $(4.393 \pm 0.084) \times 10^{-5}$, is consistent with the range of $(^{26}\text{Al}/^{27}\text{Al})_0$ reported for igneous CAIs in the CV chondrites. If they formed from a nebular gaseous reservoir with homogeneous distribution of ^{26}Al , the results suggest that CAI condensation and CAI melting in a hot nebular gas continued for at least ~ 0.2 Myr at the very beginning of the Solar System. The variations in $(^{26}\text{Al}/^{27}\text{Al})_0$ among the fluffy Type A CAIs also raise an alternative possibility of heterogeneous distributions of ^{26}Al in the forming region.

Acknowledgements

We thank Ken-ichi Abe for supporting glass synthesis and Astromaterials Science Research Group of ISAS/JAXA for supporting sample preparations and FE-SEM work. We also thank Glenn MacPherson and three anonymous reviewers for their constructive comments. We are also grateful to associate editor Frederic Moynier for his constructive comments and suggestions. This work is supported by Monka-sho grants (N. Kawasaki and H. Yurimoto) and KOPRI grants PM18030(20140409) and PE19230 (C. Park).

Appendix A. Synthesis of melilite glasses for RSF

Because melilites in FTA CAIs and FGIs generally have wide variations in $^{27}\text{Al}/^{24}\text{Mg}$ ratio, we investigated the instrumental mass fractionation effects for Mg-isotopes and the RSFs for Mg and Al in melilite using synthetic melilite glasses having different $^{27}\text{Al}/^{24}\text{Mg}$ ratios (åkermanite contents, Åk): Åk6 ($^{27}\text{Al}/^{24}\text{Mg} = 39.05 \pm 0.12$) and Åk59 ($^{27}\text{Al}/^{24}\text{Mg} = 1.795 \pm 0.007$). These were synthesized from mixed powders of carbonates (CaCO_3) and oxides (MgO , Al_2O_3 , and SiO_2). Before weighing the powders, the MgO powder was heated at 1000°C for 1 h to release absorbed water. The powders were then weighed and mixed by ball milling with iron coated nylon balls in ethanol for 12 h. After drying, the

Table A.1
Chemical composition of synthesized melilite glasses.

wt%	1	2
Na_2O	0.08	0.52
MgO	0.89	8.50
Al_2O_3	34.75	15.24
SiO_2	22.14	33.65
K_2O	bdl	bdl
CaO	41.89	42.17
TiO_2	bdl	bdl
Cr_2O_3	bdl	bdl
MnO	bdl	bdl
FeO	0.02	0.02
Total	99.77	100.10
<i>Cations per 7 oxygen anions</i>		
Na	0.008	0.046
Mg	0.061	0.581
Al	1.885	0.824
Si	1.019	1.543
K	bdl	bdl
Ca	2.066	2.072
Ti	bdl	bdl
Cr	bdl	bdl
Mn	bdl	bdl
Fe	0.002	0.001
Total	5.041	5.067
Åk	6.1	58.5
$^{27}\text{Al}/^{24}\text{Mg}$	39.05	1.80

Åk: Åkermanite contents (mol%), bdl: below detection limit.

Table A.2

Al–Mg isotope data obtained for the synthesized melilite glasses.

Glass comp.	No. of EPMA meas.	$^{27}\text{Al}/^{24}\text{Mg}_{\text{EPMA}}$	2SE	No. of SIMS meas.	$^{27}\text{Al}/^{24}\text{Mg}_{\text{SIMS}}$	2SE	RSF ^a	2SE ^b	$\delta^{25}\text{Mg}_{\text{std}}^{\text{c}}$	2SE	$\delta^{26}\text{Mg}^*$	2SE
Åk6	210	39.05	0.12	6	38.82	0.07	0.994	0.004	−7.6	0.4	0.4	0.5
Åk59	20	1.795	0.007	8	1.782	0.013	0.992	0.008	−7.3	0.3	−0.2	0.4

^a $\text{RSF} = (^{27}\text{Al}/^{24}\text{Mg})_{\text{SIMS}} / (^{27}\text{Al}/^{24}\text{Mg})_{\text{EPMA}}$.

^b Analytical uncertainties of EPMA and SIMS are propagated.

^c $\delta^{25}\text{Mg}_{\text{std}} = [(^{25}\text{Mg}/^{24}\text{Mg})_{\text{std}} / (^{25}\text{Mg}/^{24}\text{Mg})_{\text{ref}} - 1] \times 1000$.

powders were calcined twice at 1000 °C, once for 20 h and once for 12 h, to decarbonate CaCO₃. The calcined powders were well pulverized by ball milling for 24 h and pressed into disks (diameter of 10 mm and thickness of 2 mm). The disks of mixed powders were fused in a Pt crucible at 1700 °C (above their respective melting temperatures, ~1580 °C for Åk6 and ~1430 °C for Åk59; Osborn and Schairer, 1941) for 1 h by a vertical tube furnace. The melt was quenched by removal of the Pt crucible from the furnace. The Pt crucible was then lowered manually into water to form glasses. The synthesized melilite glasses were embedded in epoxy and prepared as a polished mount. The polished mount of melilite glasses was coated with a ~25 nm thick carbon film to conduct charge on the sample surface. The chemical compositions of melilite glasses were studied with a field emission electron probe microanalyzer (FE-EPMA; JEOL JXA-8530F) at Korea Polar Research Institute using a 15 keV accelerating voltage, 10 nA beam current, and ~5 μm beam size using five wavelength dispersive X-ray spectrometers (WDS), which are listed in Table A.1. Natural and synthetic minerals were used as standards. Counting times were 20 s on the peak and 10 s on background, except for Na and K (10 s on the peak and 5 s on background). Atomic number (Z), absorption (A), and fluorescence (F) corrections were applied using the CITZAF phi-rho-Z matrix correction implanted in the JEOL software (Armstrong, 1995). The element detection limits determined by the JEOL software were as follows (in wt%): SiO₂ (0.02), TiO₂ (0.01), Al₂O₃ (0.01), Cr₂O₃ (0.01), FeO (0.02), MnO (0.02), MgO (0.01), CaO (0.01), Na₂O (0.01), and K₂O (0.01). The results of the Al–Mg isotope analyses in the peak-jumping mode for the synthesized melilite glasses are summarized in Table A.2. The determined RSFs of Al/Mg, $\delta^{25}\text{Mg}_{\text{std}}$, and $\delta^{26}\text{Mg}^*$ for the two glasses with different $^{27}\text{Al}/^{24}\text{Mg}$ ratios are identical within errors; no significant matrix effects for the instrumental mass fractionation and the RSFs for aluminum and magnesium are identified between the melilite glasses under the measurement conditions used here. The Åk6 melilite glass and another synthetic melilite glass (Åk40, Itoh et al., 2008; Kawasaki et al., 2017, 2018) were used for the SIMS standardizations for Al-rich melilite, while the Åk40 melilite glass was used for Al-poor melilite.

Appendix B. Supplementary material

Supplementary material related to this article can be found online at <https://doi.org/10.1016/j.epsl.2019.01.026>.

References

- Armstrong, J.T., 1995. CITZAF: a package of correction programs for the quantitative electron microbeam X-ray analysis of thick polished materials, thin-films, and particles. *Microbeam Anal.* 4, 177–200.
- Beckett, J.R., Stolper, E., 1994. The stability of hibonite, melilite and other aluminous phases in silicate melts: implications for the origin of hibonite-bearing inclusions from carbonaceous chondrites. *Meteoritics* 29, 41–65.
- Bollard, J., Connelly, J.N., Whitehouse, M.J., Pringle, E.A., Bonal, L., Jorgensen, J.K., Nordlund, A., Moynier, F., Bizzarro, M., 2017. Early formation of planetary building blocks inferred from Pb isotopic ages of chondrules. *Sci. Adv.* 3, e1700407.
- Bolsler, D., Zega, T.J., Asaduzzaman, A., Bringuier, S., Simon, S.B., Grossman, L., Thompson, M.S., Domanik, K.J., 2016. Microstructural analysis of Wark–Lovering rims in the Allende and Axtell CV3 chondrites: implications for high-temperature nebular processes. *Meteorit. Planet. Sci.* 51, 743–756.
- Boynton, W.V., 1975. Fractionation in the solar nebula – condensation of yttrium and the rare earth elements. *Geochim. Cosmochim. Acta* 39, 569–584.
- Connelly, J.N., Bizzarro, M., Krot, A.N., Nordlund, A., Wielandt, D., Ivanova, M.A., 2012. The absolute chronology and thermal processing of solids in the solar protoplanetary disk. *Science* 338, 651–655.
- Davis, A.M., Grossman, L., 1979. Condensation and fractionation of rare earths in the solar nebula. *Geochim. Cosmochim. Acta* 43, 1611–1632.
- Davis, A.M., Richter, F.M., Mendybaev, R.A., Janney, P.E., Wadhwa, M., McKeegan, K.D., 2015. Isotopic mass fractionation laws for magnesium and their effects on ^{26}Al – ^{26}Mg systematics in solar system materials. *Geochim. Cosmochim. Acta* 158, 245–261.
- Grossman, L., 1972. Condensation in the primitive solar nebula. *Geochim. Cosmochim. Acta* 86, 597–619.
- Grossman, L., Ebel, D.S., Simon, S.B., 2002. Formation of refractory inclusion by evaporation of condensate precursors. *Geochim. Cosmochim. Acta* 66, 145–161.
- Holst, J.C., Olsen, M.B., Paton, C., Nagashima, K., Schiller, M., Wielandt, D., Larsen, K.K., Connelly, J.N., Jorgensen, J.K., Krot, A.N., Nordlund, A., Bizzarro, M., 2013. ^{182}Hf – ^{182}W age dating of a ^{26}Al -poor inclusion and implications for the origin of short-lived radioisotopes in the early Solar System. *Proc. Natl. Acad. Sci. USA* 110, 8819–8823.
- Itoh, S., Makide, K., Yurimoto, H., 2008. Calculation of radiogenic ^{26}Mg of CAI minerals under high precision isotope measurement by SIMS. *Appl. Surf. Sci.* 255, 1476–1478.
- Jacobsen, B., Yin, Q.-Z., Moynier, F., Amelin, Y., Krot, A.N., Nagashima, K., Hutcheon, I.D., Palme, H., 2008. ^{26}Al – ^{26}Mg and ^{207}Pb – ^{206}Pb systematics of Allende CAIs: canonical solar initial $^{26}\text{Al}/^{27}\text{Al}$ ratio reinstated. *Earth Planet. Sci. Lett.* 272, 353–364.
- Katayama, J., Itoh, S., Yurimoto, H., 2012. Oxygen isotopic zoning of reversely zoned melilite crystals in a Fluffy Type A Ca–Al-rich inclusion from the Vigarano meteorite. *Meteorit. Planet. Sci.* 47, 2094–2106.
- Kawasaki, N., Sakamoto, N., Yurimoto, H., 2012. Oxygen isotopic and chemical zoning of melilite crystals in a Type A Ca–Al-rich inclusion of Efremovka CV3 chondrite. *Meteorit. Planet. Sci.* 47, 2084–2093.
- Kawasaki, N., Kato, C., Itoh, S., Wakaki, S., Ito, M., Yurimoto, H., 2015. ^{26}Al – ^{26}Mg chronology and oxygen isotope distributions of multiple melting for a Type C CAI from Allende. *Geochim. Cosmochim. Acta* 169, 99–114.
- Kawasaki, N., Itoh, S., Sakamoto, N., Yurimoto, H., 2017. Chronological study of oxygen isotope composition for the solar protoplanetary disk recorded in a fluffy Type A CAI from Vigarano. *Geochim. Cosmochim. Acta* 201, 83–102.
- Kawasaki, N., Simon, S.B., Grossman, L., Sakamoto, N., Yurimoto, H., 2018. Crystal growth and disequilibrium distribution of oxygen isotopes in an igneous Ca–Al-rich inclusion from the Allende carbonaceous chondrite. *Geochim. Cosmochim. Acta* 221, 318–341.
- Kawasaki, N., Yurimoto, H., 2017. Al–Mg systematics of nebular condensates in the Efremovka CV3 chondrite. In: 48th Lunar and Planetary Science Conference (abstract #1091).
- Kita, N.T., Ushikubo, T., Knight, K.B., Mendybaev, R.A., Davis, A.M., Richter, F.M., Fournelle, J.H., 2012. Internal ^{26}Al – ^{26}Mg isotope systematics of a Type B CAI: remelting of refractory precursor solids. *Geochim. Cosmochim. Acta* 86, 37–51.
- Kita, N.T., Yin, Q.-Z., MacPherson, G.J., Ushikubo, T., Jacobsen, B., Nagashima, K., Kurahashi, E., Krot, A.N., Jacobsen, S.B., 2013. ^{26}Al – ^{26}Mg isotope systematics of the first solids in the early solar system. *Meteorit. Planet. Sci.* 48, 1383–1400.
- Kööp, L., Davis, A.M., Nakashima, D., Park, C., Krot, A.N., Nagashima, K., Tenner, T.J., Heck, P.R., Kita, N.T., 2016. A link between oxygen, calcium and titanium isotopes in ^{26}Al -poor hibonite-rich CAIs from Murchison and implications for the heterogeneity of dust reservoirs in the solar nebula. *Geochim. Cosmochim. Acta* 189, 70–95.
- Krot, A.N., MacPherson, G.J., Ulyanov, A.A., Petaev, M.I., 2004. Fine-grained, spinel-rich inclusions from the reduced CV chondrites Efremovka and Leoville, I: mineralogy, petrology, and bulk chemistry. *Meteorit. Planet. Sci.* 39, 1517–1553.
- Krot, A.N., Nagashima, K., Bizzarro, M., Huss, G.R., Davis, A.M., McKeegan, K.D., Meyer, B.S., Ulyanov, A.A., 2008. Multiple generations of refractory inclusions in the metal-rich carbonaceous chondrites Acfer 182/214 and Isheyev. *Astrophys. J.* 672, 713–721.
- Krot, A.N., Makide, K., Nagashima, K., Huss, G.R., Oglione, R.C., Ciesla, F.J., Yang, L., Hellebrand, E., Gaidos, E., 2012. Heterogeneous distribution of ^{26}Al at the birth of the solar system: evidence from refractory grains and inclusions. *Meteorit. Planet. Sci.* 47, 1948–1979.

- Krot, A.N., Nagashima, K., van Kooten, E.M.M., Bizzarro, M., 2017. High-temperature rims around calcium–aluminum-rich inclusions from the CR, CB and CH carbonaceous chondrites. *Geochim. Cosmochim. Acta* 201, 155–184.
- Larsen, K.K., Trinquier, A., Paton, C., Schiller, M., Wielandt, D., Ivanova, M.A., Connelly, J.N., Nordlund, Å., Krot, A.N., Bizzarro, M., 2011. Evidence for magnesium isotope heterogeneity in the solar protoplanetary disk. *Astrophys. J. Lett.* 735, L37–L43.
- Lee, T., Papanastassiou, D.A., Wasserburg, G.J., 1976. Demonstration of ^{26}Mg excess in Allende and evidence for ^{26}Al . *Geophys. Res. Lett.* 3, 41–44.
- Lodders, K., 2003. Solar system abundances and condensation temperatures of the elements. *Astrophys. J.* 591, 1220–1247.
- Ludwig, K., 2003. *ISOPLLOT: A Geochronological Toolkit for Microsoft Excel 3.00*. Berkeley Geochronological Center Special Publication No. 4, Berkeley, CA 94709.
- MacPherson, G.J., Grossman, L., 1981. A once-molten, coarse-grained, Ca-rich inclusion in Allende. *Earth Planet. Sci. Lett.* 52, 16–24.
- MacPherson, G.J., Grossman, L., Allen, J.M., Beckett, J.R., 1981. Origin of rims on coarse-grained inclusions in the Allende meteorite. In: *Proceedings of the 12th Lunar and Planetary Science Conference*, pp. 1079–1091.
- MacPherson, G.J., Grossman, L., 1984. Fluffy Type A Ca-, Al-rich inclusions in the Allende meteorite. *Geochim. Cosmochim. Acta* 48, 29–46.
- MacPherson, G.J., Davis, A.M., Zinner, E.K., 1995. The distribution of aluminum-26 in the early Solar System – a reappraisal. *Meteoritics* 30, 365–386.
- MacPherson, G.J., Bullock, E.S., Janney, P.E., Kita, N.T., Ushikubo, T., Davis, A.M., Wadhwa, M., Krot, A.N., 2010. Early solar nebular condensates with canonical, not supracanonical, initial $^{26}\text{Al}/^{27}\text{Al}$ ratios. *Astrophys. J. Lett.* 711, L117–L121.
- MacPherson, G.J., Kita, N.T., Ushikubo, T., Bullock, E.S., Davis, A.M., 2012. Well-resolved variations in the formation ages for Ca–Al-rich inclusions in the early Solar System. *Earth Planet. Sci. Lett.* 331–332, 43–54.
- MacPherson, G.J., 2014. Calcium–aluminum-rich inclusions in chondritic meteorites. In: Davis, A.M. (Ed.), *Meteorites and Cosmochemical Processes*. In: *Treatise on Geochemistry*, vol. 1. Elsevier, Oxford, pp. 139–179.
- MacPherson, G.J., Bullock, E.S., Tenner, T.J., Nakashima, D., Kita, N.T., Ivanova, M.A., Krot, A.N., Petaev, M.I., Jacobsen, S.B., 2017. High precision Al–Mg systematics of forsterite-bearing Type B CAIs from CV3 chondrites. *Geochim. Cosmochim. Acta* 201, 65–82.
- Makide, K., Nagashima, K., Krot, A.N., Huss, G.R., Ciesla, F.J., Hellebrand, E., Gaidos, E., Yang, L., 2011. Heterogeneous distribution of ^{26}Al at the birth of the solar system. *Astrophys. J. Lett.* 733, L31–L34.
- Norris, T.L., Gancarz, A.J., Rokop, D.J., Thomas, K.W., 1983. Half-life of ^{26}Al . *J. Geophys. Res.* 88, B331–B333.
- Osborn, E., Schairer, J.F., 1941. The ternary system pseudowollastonite–åkermanite–gehlenite. *Am. J. Sci.* 239, 715–763.
- Park, C., Wakaki, S., Sakamoto, N., Kobayashi, S., Yurimoto, H., 2012. Oxygen isotopic variations of melilite crystals in a Type A CAI from Allende. *Meteorit. Planet. Sci.* 47, 2070–2083.
- Park, C., Nagashima, K., Krot, A.N., Huss, G.R., Davis, A.M., Bizzarro, M., 2017. Calcium–aluminum-rich inclusions with fractionation and unidentified nuclear effects (FUN CAIs), II: heterogeneities of magnesium isotopes and ^{26}Al in the early Solar System inferred from in situ high-precision magnesium-isotope measurements. *Geochim. Cosmochim. Acta* 201, 6–24.
- Simon, J.I., Young, E.D., Russell, S.S., Tonui, E.K., Dyl, K.A., Manning, C.E., 2005. A short timescale for changing oxygen fugacity in the solar nebula revealed by high-resolution ^{26}Al – ^{26}Mg dating of CAI rims. *Earth Planet. Sci. Lett.* 238, 272–283.
- Villeneuve, J., Chaussidon, M., Libourel, G., 2009. Homogeneous distribution of ^{26}Al in the solar system from the Mg isotopic composition of chondrules. *Science* 325, 985–988.
- Wark, D.A., Lovering, J.F., 1977. Marker events in the early solar system: evidence from rims on Ca–Al-rich inclusions in carbonaceous chondrites. In: *Proceedings of the 8th Lunar and Planetary Science Conference*, pp. 95–112.
- Wark, D.A., Lovering, J.F., 1982. The nature and origin of type B1 and B2 Ca–Al-rich inclusions in the Allende meteorite. *Geochim. Cosmochim. Acta* 46, 2581–2594.
- Wark, D.A., 1987. Plagioclase-rich inclusions in carbonaceous chondrite meteorites: liquid condensates? *Geochim. Cosmochim. Acta* 51, 221–242.
- Wark, D.A., Boynton, W.V., 2001. The formation of rims on calcium–aluminum-rich inclusions: step I – flash heating. *Meteorit. Planet. Sci.* 36, 1135–1166.
- Wark, D.A., 2005. The first step in CAI rim formation: flash heating or subsolidus evaporation?. In: *36th Lunar and Planetary Science Conference (abstract #1643)*.
- Wasserburg, G.J., Lee, T., Papanastassiou, D.A., 1977. Correlated O and Mg isotopic anomalies in Allende inclusions, II: magnesium. *Geophys. Res. Lett.* 4, 299–302.
- Wasserburg, G.J., Wimpenny, J., Yin, Q.-Z., 2012. Mg isotopic heterogeneity, Al–Mg isochrons, and canonical $^{26}\text{Al}/^{27}\text{Al}$ in the early solar system. *Meteorit. Planet. Sci.* 47, 1980–1997.
- Yurimoto, H., Ito, M., Nagasawa, H., 1998. Oxygen isotope exchange between refractory inclusion in Allende and solar nebula gas. *Science* 282, 1874–1877.